Extraction of Mobility from Quantum Transport Calculations of Type-II Superlattices

Extraction of Mobility from Quantum Transport Calculations of Type-II Superlattices

John Glennon,[1,*] Francesco Bertazzi,[2] Alberto Tibaldi,[2] and Enrico Bellotti[1,3]

[1] *Division of Material Science and Engineering (MSE), Boston University, Boston, Massachusetts 02215, USA*

[2] *Department of Electronics and Telecommunications (DET), Politecnico di Torino and IEIIT-CNR, Torino 10129, Italy*

[3] *Department of Electrical and Computer Engineering (ECE), Boston University, Boston, Massachusetts 02215, USA*

(Received 10 November 2022; revised 1 March 2023; accepted 13 March 2023; published 17 April 2023)

Type-II superlattices (T2SLs) are being investigated as an alternative to traditional bulk materials in infrared photodetectors due to predicted fundamental advantages. Subject to significant quantum effects, these materials require the use of quantum transport methodologies, such as the nonequilibrium Green's function (NEGF) formalism to fully capture the relevant physics without uncontrolled approximations. Carrier mobility is a useful parameter that affects carrier collection in photodetectors. This work investigates the application of mobility extraction methodologies from quantum transport simulations in the case of T2SLs exemplified using an InAs/GaSb midwave structure. In a resistive region, the average velocity can be used to calculate an apparent mobility that incorporates both diffusive and ballistic effects. However, the validity of this mobility for predicting device properties is limited to cases of diffusive limited transport or when the entire device can be included in the simulation domain. Two methods that have been proposed to extract diffusive limited mobility, one based on approximating the ballistic component of transport and the other which considers the scaling of resistance with simulation size, were also studied. In particular, the resistance scaling approach is demonstrated to be the method most physically relevant to predicting macroscopic transport. We present a method for calculating the mobility from resistance scaling considerations that accounts for carrier density variation between calculations, which is particularly relevant in the case of electrons. Finally, we comment on the implications of applying the different mobility extraction methodologies to device property predictions. The conclusions of this study are not limited to T2SLs, and may be generally relevant to quantum transport mobility studies.

DOI: 10.1103/PhysRevApplied.19.044045

I. INTRODUCTION

Semiclassical models, such as drift diffusion (DD) or the Boltzmann transport equation (BTE) have been successfully employed to predict semiconductor materials properties and device performance for decades. However, as device features have continued to shrink, the need for methods that capture the relevant physics has led to the development of fully quantum mechanical methods for simulating device properties. One of the most useful approaches is the nonequilibrium Green's function (NEGF) formalism [1]. NEGF calculations can be used to evaluate one-particle properties, such as currents and carrier densities directly from Green's functions. However, carrier mobility, a key transport parameter used in many semiclassical device models, is not germane to the NEGF formalism and requires special considerations. The motivation for extracting mobility from NEGF calculations is to provide a bridge between the nanometer-scale phenomena of transport in semiconductor structures with macroscopic device properties. The extracted mobility from NEGF calculations can be used in quantum corrected DD transport models [2–5], which are computationally more efficient. These include approaches such as Schrodinger-Poisson DD [6] and landscape-localization DD [7,8].

A significant amount of literature has been devoted to the extraction of carrier mobility from quantum transport calculations [9–20]. Different methods have been used to achieve this goal, but they are not always equivalent, and may lead to different mobility values and electric field dependencies. One method posits that the mobility can be derived from the calculated average carrier velocity as in a resistive region [19,20]. In this case, only one value of mobility is calculated to describe the transport in the simulation domain. However, theoretical mobility

*jglennon@bu.edu

predictions [20–28] and experimental evidence [29–35] for nanoscale devices demonstrating a degradation in the apparent mobility suggest that the use of the macroscopic mobility becomes questionable at this scale. In consideration of these developments, a method of mobility extraction evolved from the model introduced by Shur [21] that uses a concept called the "ballistic mobility" to incorporate the effects of ballistic transport. This model, which is sometimes referred to in the literature as "Shur's model," generally incorporates an approximation for the ballistic mobility either from analytical methods [21,22,24,28,35] or extracted from a purely ballistic simulation [9–11,14, 23,36]. The literature focusing on extracting mobility from quantum transport calculations has focused on the latter method [9–11,14]. It is worth noting that Shur proposed his model only to "crudely illustrate" the impact that ballistic effects can have on mobility [21]. For the purposes of this paper, we refer to this procedure as the "ballistic approximation" method.

Additionally, mobility can be extracted from quantum transport calculations using resistance scaling methods [12–16,18]. Niquet and co-workers present an approach that extracts the long-channel mobility (i.e., the mobility associated with an arbitrarily long device) from quantum transport calculations of nanowire field-effect transistors (FETs) and avoids approximations related to contact resistance and ballistic effects [17]. They note that while this approach avoids uncontrolled approximations, it is only valid under the condition of the channel being "long-enough" such that the intrinsic diffusive processes are well represented within the simulation domain. As devices shrink, the scattering processes may deviate in character from those of macroscopic devices. Therefore, each mobility method mentioned above should be carefully considered and used within the simulation context in which they were derived.

Much of the literature dealing with mobility extraction from quantum transport calculations focuses on FET architectures in which the entire device can be simulated from source to drain [9–18]. Among these studies, Frey and co-workers compared the results and discussed the validity of the Kubo-Greenwood, resistance scaling, and the ballistic approximation methods in the context of nanowire FETs [14]. However, NEGF-informed mobility models are also useful for nanostructured materials such as T2SLs [19,20].

T2SLs are a useful class of quantum structures based on III-V and other semiconductor materials that are being investigated as an alternative to the more established II-VI bulk material system for use in IR photodetection [37]. The drive towards III-V SLs stems from predicted advantages over the more established bulk materials, which include theoretically lower Auger recombination rates [38], higher chemical stability due to stronger bonding [37], and lower costs given the large existing industrial base for these materials [39]. However, the promise of superior performance has yet to be realized [40].

Mobility, along with carrier lifetime, is a component of diffusion length that can affect carrier collection in photodetectors. Current experimental studies of Ga-free T2SLs have shown that for detectors operating both in the long and midwave IR spectral range, hole mobility decreases with temperature [41,42]. Furthermore, a recent theoretical study by several of the authors of this paper has shown that this behavior is associated with unavoidable structural disorder [20]. While several theoretical mobility studies of T2SLs derived from quantum transport calculations have been performed [19,20], there has yet to be a comprehensive comparison of the different quantum-transport-based mobility extraction methodologies specifically applied to T2SLs.

The challenge of modeling transport in T2SL photodetectors using NEGF is that the full photodetector structure is typically on the order of several micrometers [37] due to the need to compromise between enhancing absorption and accommodating carrier diffusion lengths. However, the simulation domain of NEGF is limited by the computational requirements of the formalism. Therefore, one strategy for predicting device properties is to calculate the mobility in a small model of the SL absorber structure with the assumption that the results can be extrapolated to the larger device. Thus, quantum transport simulations of T2SL IR materials require different considerations than full-scale FET devices when extracting mobility. Furthermore, the utility of using quantum corrected semiclassical models with NEGF-derived parameters is emphasized by this limitation.

In this work, we investigate the application of the three mobility models outlined above to NEGF calculations of T2SLs, exemplified through the use of a midwave InAs/GaSb SL structure, elucidating the physical interpretation of each method, which may be relevant to applications beyond that of T2SLs.

The paper is organized as follows: the transport model along with the three mobility calculation methodologies will be presented in Sec. II. In Sec. III, the results of mobility calculations using each method will be examined and the applicability of each method for investigating electron and hole transport in T2SLs as well as the implications for predicting photodetector device properties is discussed. Finally, a summary of the findings is presented in Sec. IV.

II. METHODS

We use a fully quantum mechanical treatment of carrier transport within the NEGF formalism. A more comprehensive description of the transport model used in this work was presented in Ref. [19], but the major points are

summarized in this section. A 4×4 $k \cdot p$ Hamiltonian, which includes the first conduction, heavy-hole, light-hole, and spin-orbit split-off bands formulated within the axial approximation is used to describe the complex band structure of the T2SLs. A finite-element implementation is used in which the envelope functions are expanded in first-order Lagrange polynomials. The Luttinger parameter set from Ref. [43] is chosen for the description of the InAs and GaSb band structures. The effect of strain on the band structure is included in the 4×4 $k \cdot p$ Hamiltonian as described in Ref. [44].

For computational efficiency, we limit the treatment to transport in the growth direction only. We implement open boundary conditions at the extremes of the simulation domain through the inclusion of a self-energy term calculated via the complex band structure of the reservoirs. Using additional nonlocal self-energy terms, we introduce acoustic (ACO) and polar-optical (POP) phonon scattering in the simulations in the deformation potential and Fröhlich formalisms, respectively. The total self-energy Σ is the sum of each component. Green's functions are calculated via the Dyson and Keldysh equations [19,45]:

$$G^R(z_1, z_1', E) = G_0^R(z_1, z_1', E) + \int dz_2 \int dz_3 G_0^R(z_1, z_2, E)\Sigma^R(z_2, z_3, E)G^R(z_3, z_1', E), \tag{1}$$

$$G^{\lessgtr}(z_1, z_1', E) = \int dz_2 \int dz_3 G^R(z_1, z_2, E)\Sigma^{\lessgtr}(z_2, z_3, E)G^A(z_3, z_1', E), \tag{2}$$

which are solved via the self-consistent Born approximation (SCBA) [19].

The self-consistent solution of the Dyson and Keldysh equations are computationally prohibitive in real space, so we approximate the calculation of the self-energies using a problem-matched mode-space methodology. A new basis set is selected from the eigenstates of the noninteracting Hamiltonian within a specified energy range relevant to the transport domain being investigated. To maintain current conservation, the influence of the excluded eigenstates is folded into the problem through another self-energy term [46]. Once self-consistency is achieved, the self-energy is converted back to real space and a final calculation of the Dyson and Keldysh equations is performed. From Green's functions calculated in real space, the one-particle properties can be extracted. Of relevance to this study, the electron (hole) carrier and current densities can be calculated via [19,45,47]

$$n(z), p(z) = (\mp)\frac{i}{A}\sum_{\bar{k}} \int \frac{dE}{2\pi} G^{\lessgtr}(z, z, \bar{k}, E), \tag{3}$$

$$J_{n,p}(z) = \lim_{z' \to z} \frac{e\hbar}{m_0}\left(\frac{\partial}{\partial z} - \frac{\partial}{\partial z'}\right)\frac{1}{A}\sum_{\bar{k}} \int \frac{dE}{2\pi} G^{\lessgtr}(z, z', \bar{k}, E). \tag{4}$$

As mentioned in Sec. I, the concept of mobility is not straightforward in a quantum transport calculation; however, there have been a few methods used in the field to extract mobility from NEGF.

A. Average velocity method

For transport in a resistive region, the electron and hole mobilities can be extracted from NEGF calculations using the average of the carrier drift velocity, $v_{n,p}$ [19,20]:

$$v_{n,p} = \langle \frac{J_{n,p}}{\mp en} \rangle, \tag{5}$$

where the carrier mobility is then calculated via

$$\mu_{n,p} = \frac{v_{n,p}}{F}. \tag{6}$$

$J_{n,p}$ is the carrier current, e the elementary charge, F the applied electric field in the growth direction, and n represents the carrier density. To simplify the expressions, we use n to represent either electron or hole densities based on the given context.

B. The ballistic approximation method

In this method, the mobility that represents the transport at the nanometer scale is referred to as the "apparent mobility." Assuming a Matthiessen's rule relationship, the apparent mobility μ_{app} is separated into two components [21]:

$$\frac{1}{\mu_{\text{app}}} = \frac{1}{\mu_{\text{ball}}} + \frac{1}{\mu_{\text{diff}}}, \tag{7}$$

where μ_{ball} is the so-called "ballistic mobility" and μ_{diff} is the "diffusive mobility." We obtain an approximate value of the ballistic mobility from a NEGF calculation without the ACO and POP scattering self-energies. Then, we calculate the diffusive, or scattering-limited, mobility via Eq. (7). We note that Matthiessen's rule is not generally valid [48]. Its use for separating the ballistic component from the diffusive component has been demonstrated to be questionable at high bias [22] as well as in a nonhomogeneous nanowire FET at low bias [14].

C. Resistance scaling analysis

The last method for calculating mobility that we consider involves studying the dependence of the resistance on the device length. We follow the method outlined in

Ref. [17], which involves fitting the resistance R in the device calculated via Ohm's law to the following equation:

$$R(L) = R_c + R_B + \frac{L}{n\mu e}, \tag{8}$$

where L is the device length, n is the average carrier density in the SL, e the fundamental charge, and R_c and R_B are the contact and ballistic resistances, respectively. For the model to be valid, the resistance must vary linearly with the simulated SL length and the carrier density in the SL must be consistent between calculations. If so, we extract the "intrinsic mobility" from the slope of the resistance curve according to Eq. (8). In this work we refer to "intrinsic mobility" as equivalent to the macroscopic definition of mobility in a diffusive-limited transport. However, as we discuss in Sec. III C, it is challenging to produce calculations at different lengths with identical carrier density, particularly at low temperatures. To compensate, we use an alternative method in which we fit a linear curve to the product nR following:

$$nR(L) = nR_c + nR_B + \frac{L}{\mu e}. \tag{9}$$

This method assumes that, within the range of carrier densities exhibited in our simulations, R_c and R_B have an inversely proportional relationship with carrier density n such that $nR_c + nR_B$ is constant. For example, in the Drude model, resistance is inversely proportional to the carrier density. Furthermore, in Appendix B we derive the ballistic resistance in a three-dimensional (3D) bulk resistor with parabolic bands, which we demonstrate to be inversely proportional to carrier density for nondegenerate doping:

$$R = \frac{\sqrt{2\pi m^* K_B T}}{nq^2} \frac{F_{1/2}(\eta_F)}{F_0(\eta_F)}. \tag{10}$$

Thus, the assumptions inherent in Eq. (9) are valid for nondegenerate 3D bulk materials in the ballistic and diffusive limits. While valid for bulk materials, we demonstrate in Sec. III C that this is a reasonable approximation for hole transport within the range of carrier densities investigated.

III. RESULTS AND DISCUSSION

To probe the validity and physical interpretations of the three mobility methods in the context of Ga-based T2SL we use a prototype SL consisting of a defined number of unit cells of InAs and GaSb layers, each with thicknesses of 3 nm, assumed to be lattice matched to a GaSb substrate. Consequently, the InAs layer is in a state of tensile strain. In Fig. 1, we report the electronic structure of this SL, computed using the 4×4 $k \cdot p$ model with Bloch boundary conditions. The plots in this paper are generated in MATLAB [49] and standardized using the toolbox in Ref. [50]. We

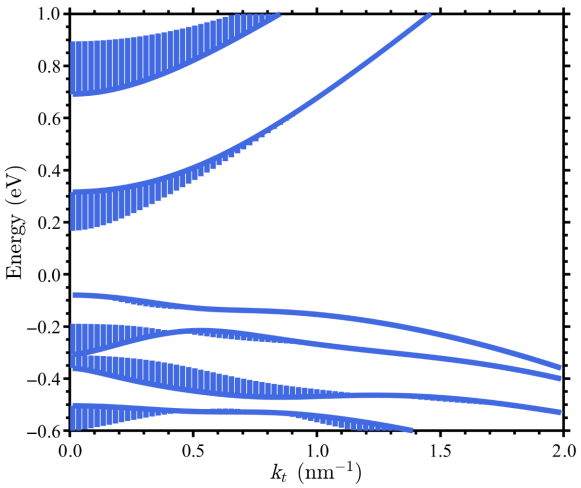

FIG. 1. Calculated energy band structure of a 3/3-nm InAs/GaSb SL plotted as a function of the transverse wave vector and modified with vertical lines representing the dispersion in the vertical wave vector. The band gap results in a cutoff wavelength of approximately 5 μm indicating that this is a MWIR SL structure.

choose the layer thicknesses to produce a nominal cutoff wavelength of approximately 5 μm, which is in the midwave IR regime. The dispersion in the growth direction is represented by vertical lines stemming from the energy of the corresponding in-plane wave number k_t, which provides an estimate for the miniband width for a given value of k_t. It is immediately apparent that the top heavy-hole miniband is very narrow compared to the first conduction miniband. This implies that the transport of holes in the growth direction will differ significantly compared with that of electrons.

In this work we choose to analyze the transport properties and benchmark the mobility models assuming an ideal SL structure (i.e., no lattice disorder). Ideal SLs exhibit transport that has more coherent character in the investigated regime relative to identical calculations where lattice disorder is included [20]. As we discuss in Sec. III E, a simulation that is dominated by coherent transport will require a larger SL structure than one dominated by diffusive transport to be able to predict the mobility of a macroscopic sample of the SL. As a result, we select an ideal SL structure to exemplify the limitations of the mobility calculation methodologies.

To extract the mobility for both carrier species we perform a series of NEGF transport calculations on finite-size SLs. As a result of the open boundary conditions at the ends of the simulation domain, electron and hole calculations are performed using different contact materials. Specifically, we select contact layers at both ends of the SL that present barriers to injection and extraction of electrons (holes) for hole (electron) transport calculations. For hole transport, we choose GaSb as the contact material, but the

choice in the case of electrons is not as straightforward. If InAs is selected, carrier injection near the contact regions makes the differentiation between the free electron and hole populations challenging in a multiband context. Thus, we select the quaternary alloy $GaSb_{0.10}[InAs_{0.91}Sb_{0.09}]_{0.90}$, which is lattice matched to GaSb [51] and avoids these complications. We note that the contact materials are not meant to be representative of a specific device, but rather we use them to probe the intrinsic properties of the T2SL being investigated. Using the calculated band structure, as in Fig. 1, we calculate the Fermi energy at equilibrium for the SL so that the target carrier has a concentration of approximately 2×10^{16} cm^{-3} in the SL region. We perform NEGF calculations for electrons and holes at different temperatures, electric field strengths in the growth direction, and number of SL periods and then compare results using the different mobility calculation techniques. See the Supplemental Material for further information regarding both the material and the discretization parameters used in each calculation that follows [52].

Prior to presenting the results, it is worthwhile to clarify some terminology regarding "convergence." In regard to the convergence of the SCBA, this is determined by the achievement of constant current throughout the simulation domain. We present only results from simulations that have achieved "convergence" in this sense. In terms of the simulation parameters, such as energy grid and spatial grid densities, there is another definition of "convergence," which refers to choosing strict enough parameters to achieve physical accuracy. This is referenced in this paper as convergence with respect to the simulation parameters. Finally, given that the macroscopic definition of mobility in diffusive-dominated transport is an intrinsic property, one could imagine another definition for "convergence," that refers to increasing the thickness of the device between the contacts until the extracted mobility reaches a constant value. In this case, we do not use the word "convergence" so as to avoid confusion, but specifically mention a failure to reach a constant mobility with respect to simulation size.

Moreover, we must also clarify the use of various terms for the mobility as used throughout this discussion. The concept of mobility breaks down in a quasiballistic regime of transport; however, the goal of this investigation is to extract useful results from calculations exhibiting a nonnegligible proportion of ballistic transport. In Sec. III D, we demonstrate that the effective mobility extracted from small structures can be shown to consist of both a diffusive component that may represent the true diffusive mobility and another term that represents small-device effects. Thus providing some validity to applying the concept proposed in Eq. (7) to this investigation. The mobility term that we use to describe this effective mobility is the "apparent mobility." We refer to the components of this apparent mobility as "ballistic" and "diffusive" mobilities, generally. The ballistic mobility encompasses the small-device effects, while the diffusive mobility encompasses the effects due to diffusive scattering. Finally, we use the term "intrinsic mobility" to represent the valid definition of mobility in a diffusive-dominated regime that is independent of simulation size. The diffusive and intrinsic mobilities should be identical in the limit of large simulation size. However, as demonstrated in Sec. III C, the behavior of the diffusive processes may depend on simulation size as well, necessitating the distinction between diffusive and intrinsic mobilities.

In Sec. III A we report the results of carrier mobilities calculated using the average velocity method for different temperatures, and device lengths. Furthermore, Secs. III B and III C present the mobilities calculated using the ballistic approximation method and the resistance scaling analysis, respectively. Based on these results, in Sec. III D we explore the relationship between the mobilities calculated in Secs. III A, III B, and III C. To conclude, we discuss the implication these results have on predicting the properties of large T2SL devices in Sec. III E.

A. Average velocity method

We compute the apparent vertical mobility from the average velocity under the assumption of drift-dominated transport [Eqs. (5) and (6)] as a function of temperature and report the results in Fig. 2 for electrons and holes [53]. The simulated SLS consists of 33 repeating SL periods plus each contact resulting in a simulation that is 200 nm long. The first thing that is noticeable is that the hole mobilities are an order of magnitude lower than the electron mobilities, which is expected given the higher hole effective mass and narrow miniband width of our structure (Fig. 1) and given the reported experimental mobilities of InAs/GaSb structures [54].

The electron (hole) mobility decreases monotonically from approximately 6 000 cm^2 V^{-1} s^{-1} (500 cm^2 V^{-1} s^{-1}) to 2800 cm^2 V^{-1} s^{-1} (70 cm^2 V^{-1} s^{-1}) as temperature increases from 30 to 200 K. The electron and hole mobility data exhibit different temperature dependencies, which suggest different transport behavior. These trends can be compared qualitatively to that of bulk material in the regimes of coherent and diffusive transport. The low-temperature behavior is likely evidence of coherent transport in these SLs. We can probe the bulk coherent regime using the analytical expression we derive (see Appendix A) for the mobility of a 3D bulk device with parabolic bands and constant effective mass under ballistic transport:

$$\mu_{\text{ball}} = \frac{L v_T}{2\,(K_B T/q)} \frac{\mathcal{F}_0(\eta_F)}{\mathcal{F}_{1/2}(\eta_F)}, \tag{11}$$

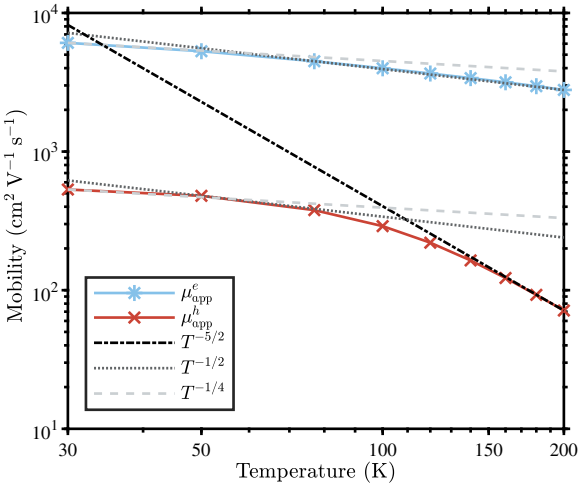

FIG. 2. The apparent vertical electron (blue line with asterisks) and hole (red line with x's) mobility as a function of temperature calculated using the average velocity method for a 200-nm MWIR T2SL with an electric field of strength 2000 V cm^{-1} (100 V cm^{-1}). The electron mobility suggests coherent transport throughout the temperature range, while the hole mobility appears to transition from coherent to diffusive dominant transport at approximately 100 K.

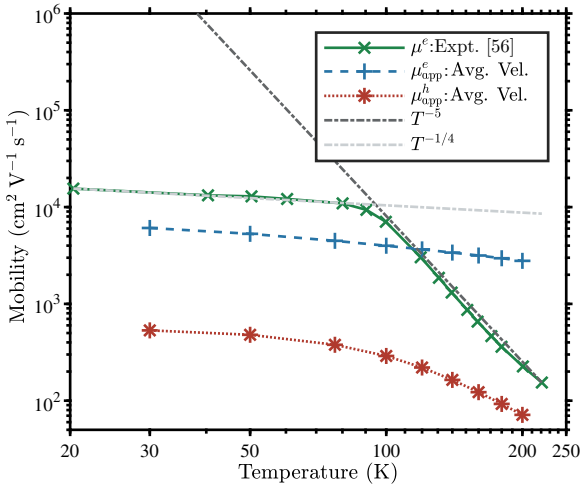

FIG. 3. The vertical electron mobility as a function of temperature (green line with x's) for an approximately 4.3-μm LWIR SL as reported by Swartz and Myers [56]. Also plotted are the apparent vertical electron (blue dashed line with pluses) and hole (red dotted line with asterisks) mobilities calculated using the average velocity method for a 200-nm MWIR T2SL. The experimental mobility transitions from a T$^{-1/4}$ to a T^{-5} dependence at approximately 90 K suggesting a qualitatively similar transition between coherent and diffusive transport as with the calculated hole mobility.

where v_T is the unidirectional thermal velocity:

$$v_T = \sqrt{\frac{2k_BT}{\pi m^*}}, \tag{12}$$

and $\eta_F = (E_F - E_c)/(k_BT)$. We use this model only for a qualitative comparison with our results. Given the very small temperature dependence of the Fermi integrals term for nondegenerate doping we see that the temperature dependence of the expression is nearly T$^{-1/2}$. This provides context for the temperature dependencies exhibited in Fig. 2 for electrons and holes. Electron mobilities exhibit a temperature dependence that is near the T$^{-1/2}$ dependence of bulk ballistic transport, while hole mobility exhibits a transition from nearly a T$^{-1/4}$ dependence to one that approaches T$^{-5/2}$. This suggests that electrons exhibit coherent dominated transport throughout the temperature range investigated, while holes transition from coherent dominated to diffusive dominated transport. The T$^{-5/2}$ trend for hole mobility at higher temperatures is likely due to POP scattering dominated transport, which is similar to the temperature dependence predicted for POP scattering of electrons in InAs (approximately T$^{-11/5}$ [55]), while the T$^{-1/4}$ dependence could be due to either a deviation in bulklike behavior or the Fermi integral terms due to degenerate doping. A qualitatively similar transition in transport regimes from low to high temperature is evident in the experimental vertical electron mobility reported by Swartz and Myers [56] for a nearly approximately 4.3 μm SL layer, which is reproduced in Fig. 3.

The experimental data exhibits an approximately T^{-5} dependence at high temperature, while the calculated hole mobility exhibits a T$^{-5/2}$ dependence. At low temperature, the dependence of the experimental data is nearly T$^{-1/4}$, which is similar to the lowest temperature dependencies of electron and hole apparent mobilities (Fig. 2), which may suggest coherent transport is present in the experimental data at low temperature. The unexpectedly low mobility at higher temperatures in the experimental data compared with the calculated data for electrons, as well as the T^{-5} dependence, is likely due to the specific structural details of the experimental device not included in the simulation. The non-negligible influence of coherent transport in these calculations has implications for the average velocity method calculation of mobilities and the applicability of this method for predicting intrinsic material properties.

As demonstrated in the expression for ballistic mobility [Eq. (11)] the ballistic component of the mobility exhibits a proportional relationship with simulation length. Thus, the apparent mobility being calculated by this method is not an intrinsic material property, but rather one dependent on the geometry of the device. Evidence of this is shown in the temperature-dependent vertical carrier mobilities presented in Fig. 4 for different simulation sizes. There is a clear length dependence in the calculated mobilities. Furthermore, the length dependence of hole mobilities is less pronounced compared with the electron mobilities at a given temperature due to hole transport being more

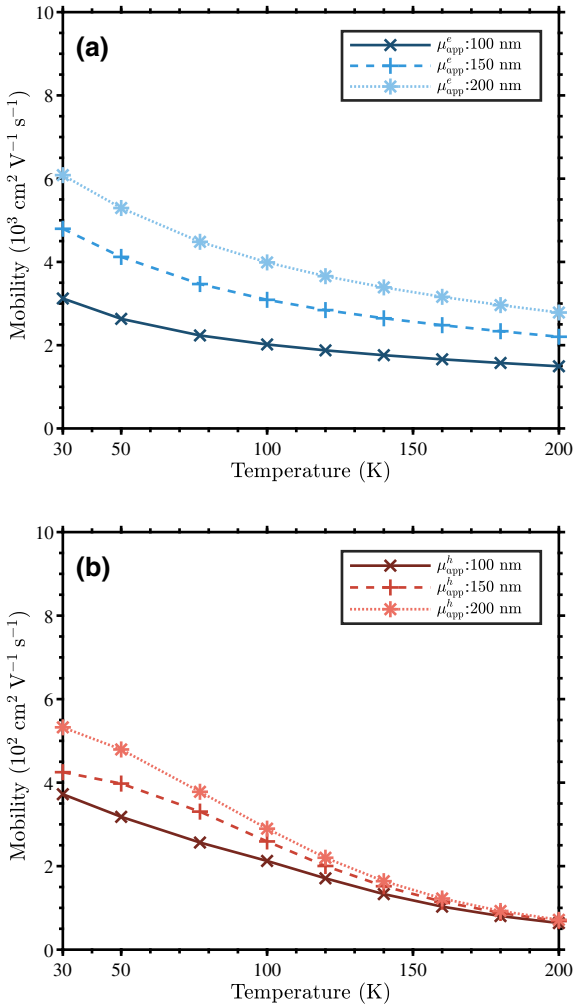

FIG. 4. The calculated apparent vertical electron (a) and hole (b) mobility as a function of temperature for different simulation sizes, as calculated via the average velocity method. The size dependence of the apparent mobility for electrons suggests strongly coherent transport, while the consistency of the hole mobilities at higher temperatures suggests coherent dominated transport.

diffusive in nature than electron transport. These results have implications for predicting properties of real devices, which are elaborated on in Sec. III E.

B. The ballistic approximation method

As mentioned in Sec. II B, the ballistic approximation provides a method for extracting ballistic and diffusive mobility components from NEGF calculations. Figures 5(a), 5(b), and 5(c) [5(d), 5(e), and 5(f)] provide electron (hole) diffusive and ballistic vertical mobilities calculated using the ballistic approximation method as a function of temperature for different simulation sizes.

Looking first at Fig. 5(c) the electron transport is shown to be nearly completely coherent throughout the temperature range we investigate for the 200-nm simulation, which is consistent with the analysis given in Sec. III A. The difference between the mobilities extracted from the diffusive and ballistic calculations is negligible resulting in very large values for the diffusive mobility. Similar results are observed in Figs. 5(a) and 5(b), as expected. However, the results for holes exhibit different behavior. There is a transition between ballistic dominated and diffusive dominated transport at decreasing temperatures for increasing simulation size. Transition temperatures occur at approximately 130, 110, and 100 K for simulation sizes of 100, 150, and 200 nm, respectively. These results are also consistent with those of Sec. III A.

There are several caveats to be made about this method. First, as mentioned in Sec. II B, it is not clear how valid Matthiessen's rule [Eq. (7)] is in the regimes investigated. If it is not valid, then the extracted mobility components could be inaccurate. Furthermore, even if Eq. (7) is valid, the diffusive mobility may be a function of the geometry at this scale, so it may not be representative of the intrinsic mobility for an infinitely large SL and instead would only represent diffusive transport in the specific geometry simulated. Finally, the mobility extracted from a ballistic calculation is not necessarily identical to the "ballistic" component of mobility in a calculation with phonon scattering. Two observations motivate this conclusion. First, when comparing the ballistic approximation method [Eq. (7)] with Eq. (8), it is clear that the ballistic mobility should incorporate the contact resistance R_c, as well as the ballistic resistance R_B, which is not captured in the ballistic calculation [28]. Also, the resistance in a ballistic calculation may not be identical to the ballistic resistance in a calculation with diffusive processes [17]. This can be exemplified by comparing the LDOS calculated with, and without, phonon scattering (see Supplemental Material [52]). Furthermore, we find that the diffusive mobility for holes at low temperatures, as well as those for electrons at all temperatures, are inconsistent when changing the simulation size. There is evidence that this inconsistency may be the result of insufficiently dense energy meshes, which are limited due to computational requirements (see Supplemental Material [52]). However, the consistency for holes at higher temperatures suggest that the ballistic approximation method may be reasonable to calculate diffusive mobility for holes under these conditions.

C. Resistance scaling analysis

As mentioned in Sec. II C, this method for calculating mobility requires that the structure be "long enough" so that the mobility exhibits intrinsic behavior resulting in the extraction of the intrinsic mobility. Given that hole transport has more diffusive character than electrons, we

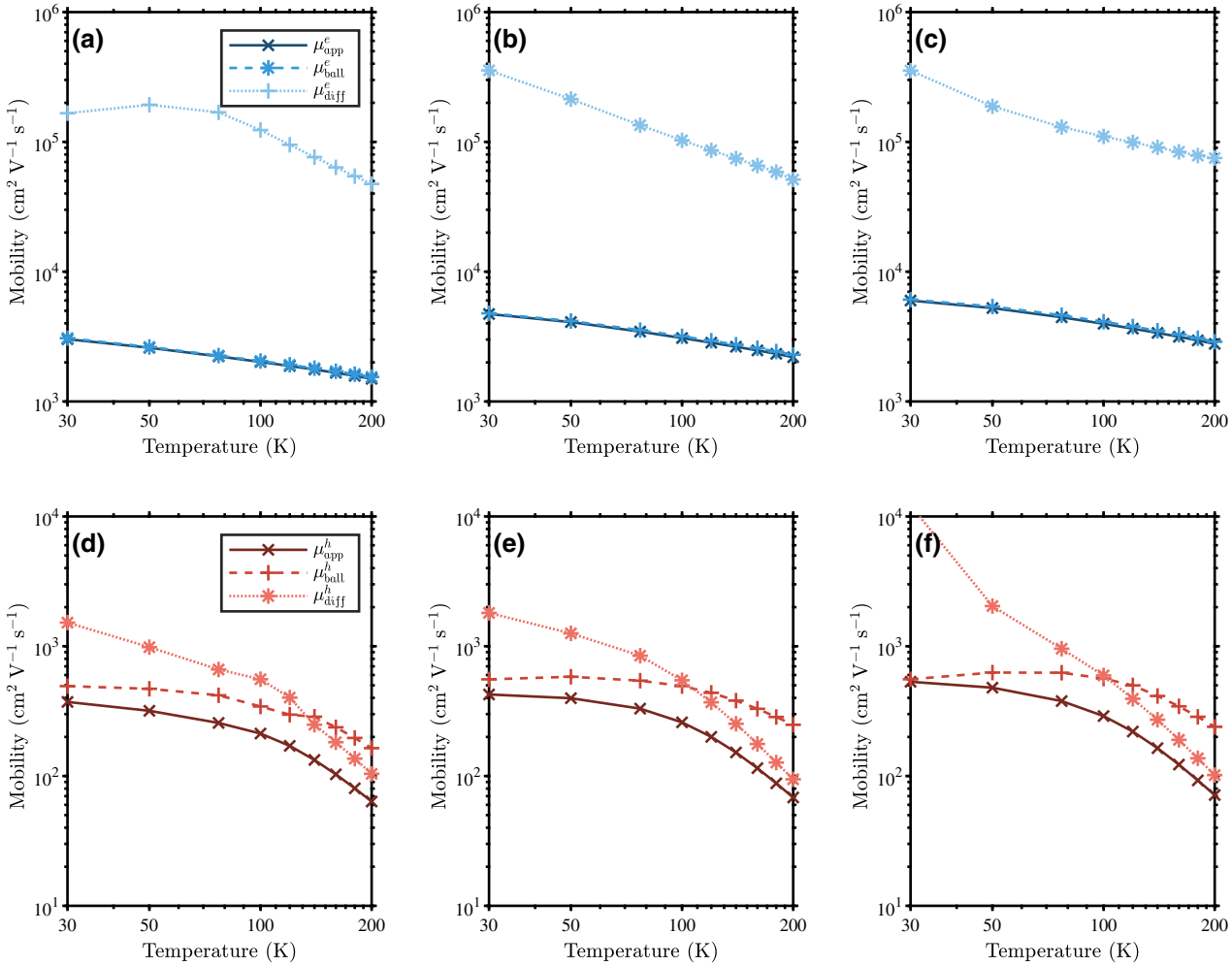

FIG. 5. The calculated vertical electron (hole) mobility as a function of temperature for simulation sizes of (a) [(d)] 100 nm, (b) [(e)] 150 nm, and (c) [(f)] 200 nm, respectively, as calculated via the ballistic approximation method. The apparent mobility (dark blue/red line with x's) is broken up into components of ballistic mobility (blue and red line with asterisks) and diffusive mobility (light blue and red line with crosses). It is demonstrated that for all simulation sizes investigated the electron transport is dominated by coherent transport throughout the temperature range. On the other hand, holes exhibit a transition between coherent dominant and diffusive dominant transport at temperatures of approximately 130 K, approximately 110 K, and approximately 100 K for simulation sizes of 100, 150, and 200 nm, respectively.

present the results for hole mobility first, as the interpretation of the results is more straightforward. Figure 6 depicts the *RA* product and hole density in the SL as a function of simulation size in the growth direction for an electric field of 100 V cm^{-1} at temperatures of 30 and 77 K. Strong linearity is demonstrated at both temperatures, but the hole density in less consistent at 30 K. We demonstrate the impact that this has on the intrinsic vertical mobility calculation by using the mean, minimum, and maximum hole densities in separate calculations of mobility using Eq. (8). We report the results in Table I. The mobility range suggested by these calculations is only a zero-order approximation. This error estimation does not take into account the impact that varying density may have on the value of the resistance. We elaborate on this when we discuss the mobility calculation for electrons later in this section.

To understand how increasing the simulation size affects the calculation, we plot in Fig. 7 the intrinsic mobilities using the mean, maximum, and minimum densities,

TABLE I. Intrinsic vertical hole mobility as calculated using the resistance scaling method for a 3/3 ML InAs/GaSb SL at 30 K with an electric field strength of 100 V cm^{-1} using the mean, maximum, and minimum hole densities, respectively, for the data set that includes the 50-, 100-, 150-, 200-, and 250-nm calculations.

	Mean density	Max density	Min density
Mobility	978	910	1 023

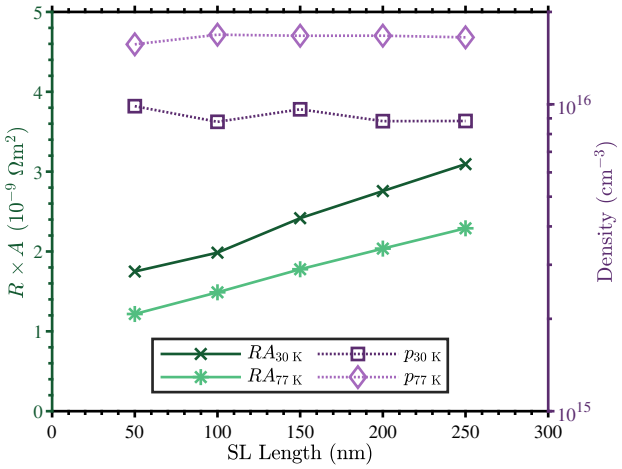

FIG. 6. The resistance-area product (green lines) and hole density (purple dotted lines), respectively, calculated for majority holes as a function of simulation size at temperatures of 30 and 77 K. Strong linearity of resistance is demonstrated at both temperatures, but the hole density is noticeably less consistent at 30 K. Linear regression on the 30 K (77 K) resistance data gives an R-squared value of 0.994 (0.999).

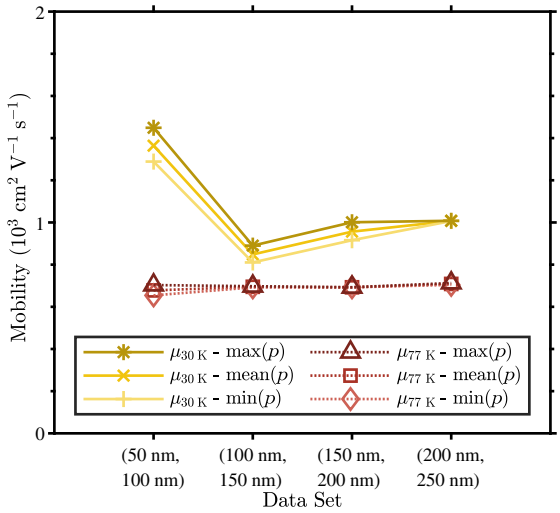

FIG. 7. The intrinsic vertical hole mobility calculated using the resistance scaling method for pairs of calculations with consecutive simulations sizes at temperatures of 30 K (yellow lines) and 77 K (red dotted lines). The mobility is calculated using three different values for the hole density: the maximum, the mean, and the minimum of the two calculations in the pair.

respectively, for consecutive pairs of data points. We find that for the 30-K data set both the average and the estimated error range of the mobility varies between pairs due to the density variation between calculations. This is a persistent issue for low-temperature calculations, which we posit is related to convergence issues with respect to the simulation parameters. These results demonstrate that while the SL appears to be long enough to achieve a linear resistance with respect to device size, the density variability may lead to sizable errors in the mobility calculation. These issues persist for the mobilities extracted for all pairs of simulation sizes excluding the 200- and 250-nm calculation. As temperature increases, so does the scattering, so we can expect the consistency of the hole densities to improve for higher temperature calculations. To demonstrate this, we perform the same analysis at 77 K and include the results in Fig. 7. We find that for all consecutive pairs of calculations the mean and error range for the intrinsic hole mobility are consistent. This demonstrates the validity of this method down to the 50-nm simulation size at 77 K.

In Fig. 8 we plot the intrinsic vertical hole mobility calculated using Eq. (8) as a function of temperature with error bars representing the estimated error range [57]. The small error bars throughout the temperature range demonstrate the consistency of the density in the simulations used to calculate the mobilities, suggesting that the results are valid.

The electron transport in this SL is more coherent in nature than the hole transport. Unlike the resistance in the hole calculations, the resistance in the electron calculations does not depend linearly on simulation size in the 100–400 nm range for an electric field strength of 100 V cm^{-1} (see Supplemental Material [52]). Thus, we

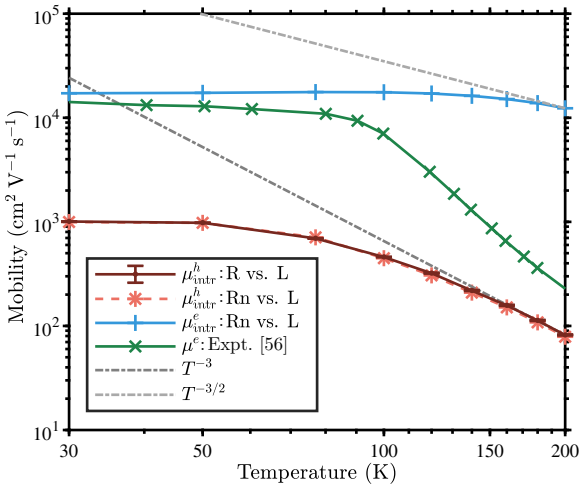

FIG. 8. The intrinsic vertical mobility as a function of temperature for a MWIR InAs/GaSb SL calculated using the resistance scaling method from quantum transport simulations by using Eq. (8) (dark red line with error bars) and Eq. (9) (light red dashed line with asterisks) for holes. Also plotted is the vertical mobility for electrons calculated using Eq. (9) (blue line with pluses). Finally, the experimentally obtained electron vertical mobility as a function of temperature (green line with x's) for an approximately 4.3-μm LWIR SL as reported by Swartz and Myers [56].

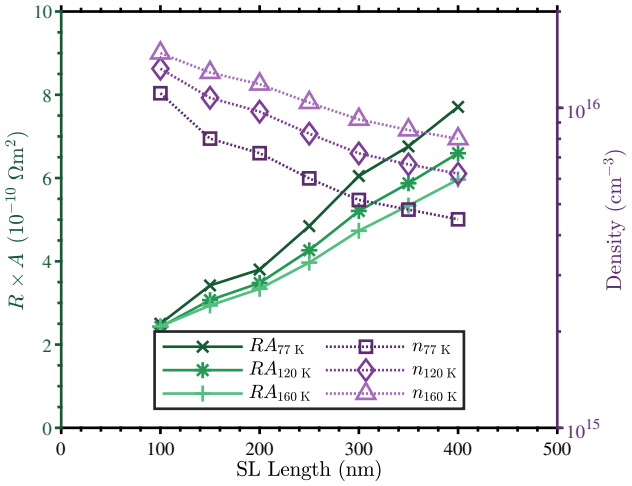

FIG. 9. The resistance-area product (green lines) and electron density (purple dotted lines), respectively, calculated for majority electrons as a function of simulation size at temperatures of 77, 120, and 160 K. Linear regression on the resistance results in *R*-squared values of 0.990, 0.992, and 0.993, respectively. There is strong linearity at all temperatures, but the electron density inconsistency suggests that resistance scaling using Eq. (8) will not be accurate for electrons.

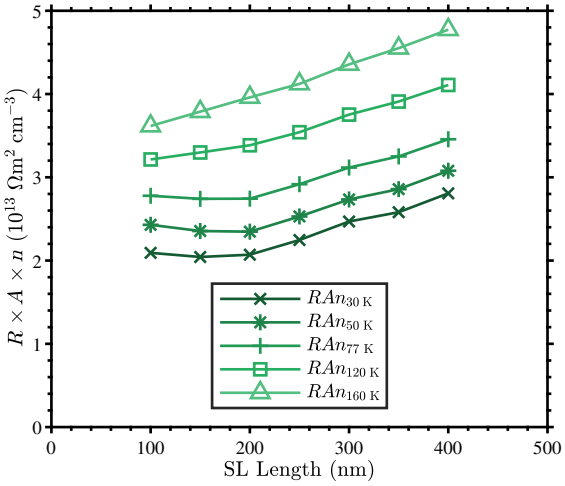

FIG. 10. The resistance-area-density product calculated for majority electrons as a function of simulation size at several temperatures. Linear regression is performed on the calculations with lengths of 200 nm and greater returning *R*-squared values of 0.992, 0.995, 0.997, 0.998, and 0.997, respectively, suggesting that valid mobilities may be extracted using Eq. (9).

increase the electric field strength to 2000 V cm^{-1} for our vertical electron mobility calculations. Figure 9 presents the *RA* product for electrons as a function of simulation size. The strong linearity suggests that the resistance scaling method may be valid at this electric field strength for electrons at temperatures of 77 K and above. However, the calculated electron density decreases monotonically with increasing simulation size. If this affect is not accounted for, the calculated mobility can have substantial error (see Supplemental Material [52]). To compensate for the inconsistent density, we use Eq. (9). In Fig. 10 we plot the *nRA* product as a function of simulation size for different temperatures. These results demonstrate that linearity is achieved for each temperature with calculation lengths of 200 nm or larger. However, the *nRA* product deviates from linearity for smaller simulations below 160 K. The cause of this behavior is evident in the behavior of POP scattering. Given that electron transport is largely ballistic, the existence of high LDOS at an energy level below the left reservoir Fermi level by the POP scattering energy is required for significant scattering to occur. For the 200-nm simulations, in which linearity of resistance begins, the Fermi levels of the left and right reservoirs are offset by 40 meV, which is larger than the POP scattering energy chosen for the scattering self-energy (30 meV) resulting in enhanced scattering.

This enhanced scattering is sufficient to impose linear scaling behavior on the calculated resistance. To demonstrate, we plot the spatially resolved spectral currents as well as the in-scattering rates associated with POP scattering for 200-nm simulations of electrons and holes at 77 K in Fig. 11. Electrons entering from the left reservoir conduct ballistically throughout most of the structure resulting in low electron in-scattering rates. However, they scatter into lower energy states near the right reservoir, which is exemplified by high in-scattering rates. This is also visible in the spatially resolved spectral current for electrons where the spectral current is nearly constant with respect to energy from left to right across the structure while demonstrating current at lower energy near the right reservoir, see inset of Fig. 11. For shorter simulation sizes, fewer states are available for the electrons to scatter into resulting in reduced POP scattering. There is evidence that the requirement of an approximately 40 meV difference in contact Fermi levels to achieve linear resistance scaling may be independent of electric field strength and simulation size (see Supplemental Material [52]). In contrast, comparing the hole in-scattering rates with the spectral current, it is clear that holes are scattering into and out of virtual states at energies above the hole miniband. Thus, POP scattering of holes is quasiperiodic away from the reservoirs. This demonstrates that POP scattering of holes far from the reservoirs is consistent for much smaller simulations. Similar plots for different simulation sizes are given in the Supplementary Material to provide more context [52].

In Fig. 8 we also plot the intrinsic vertical electron mobility calculated with Eq. (9) as a function of temperature using the *nRA* product data that has achieved strong linearity [58]. These results are plotted alongside the experimental vertical electron mobility as a function of temperature reported by Swartz and Myers [56] for

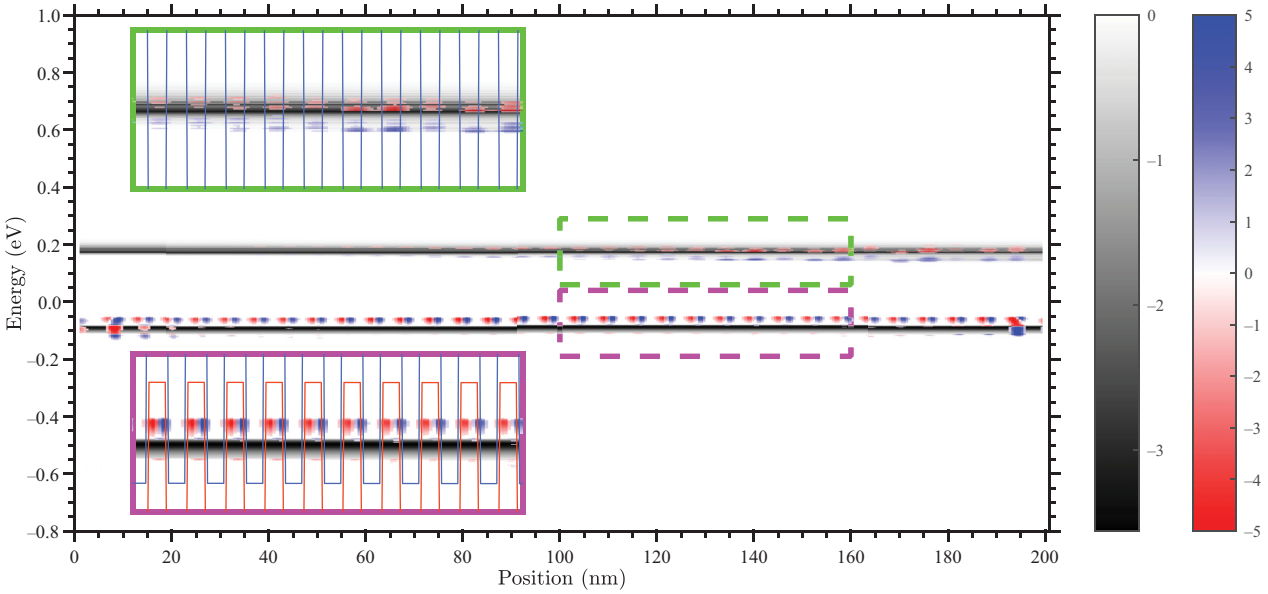

FIG. 11. The electron (data at higher energy levels) and hole (data at lower energy levels) spatially resolved spectral currents (in 10^6 Acm^{-2} and 10^4 Acm^{-2}, respectively) and in-scattering rates (in 10^{26} s^{-1} cm^{-3} and 10^{24} s^{-1} cm^{-3}, respectively) associated with POP scattering for a 200-nm simulation at 77 K. POP scattering is size dependent for electrons, but nearly size independent for holes at this scale. Note that this figure is a composite plot of two separate calculations, one for electrons and one for holes, with electric field strengths of 100 V cm^{-1} and 2000 V cm^{-1}, respectively. Thus, the SL band diagrams are only included in the two insets as they would conflict in the composite plot. (The spectral currents are displayed in a grayscale colormap while the POP in-scattering rates are displayed in a blue and red colormap.)

a nearly approximately 4.3 μm SL layer. The intrinsic electron mobility values calculated using Eq. (9) are significantly higher than the apparent mobilities calculated in Sec. III A using the average velocity method confirming that electron transport is highly coherent in these simulations. This is consistent with the results of the analyses from Secs. III A and III B. The low-temperature electron mobility is of the same order of magnitude as the experimental data (see Fig. 8), but the high temperature experimental mobility is orders of magnitude lower. As we mention in Sec. III A, this mobility degradation is likely due to specific structural details of the experimental device that are not included in the simulations. For completeness, we discuss the results of holes using Eq. (9).

In Fig. 8, for comparison with those calculated using Eq. (8), we also include the intrinsic vertical hole mobility calculated using Eq. (9) as a function of temperature. [57]. At the temperatures investigated in this study the percent difference of the intrinsic mobilities calculated using both methods is less than 5 % in magnitude. While this suggests that the assumptions of Eq. (9) are reasonable for holes at these temperatures, we cannot be certain that the assumptions hold for electrons.

D. Comparison between mobility calculation methods

As demonstrated in Sec. III A, the average velocity method calculates the apparent mobility. On the other hand, the resistance scaling analysis method calculates the intrinsic mobility. To relate these two different mobilities, we use Eq. (13) to extract an expression for the conceptual ballistic mobility that represents the $R_c + R_B$ component of the total resistance in Eq. (8) resulting in the following relation [12]:

$$\mu_{\text{ball}} = \frac{L}{ne(R_C + R_0)}. \tag{13}$$

Using this equation, along with Matthiessen's rule [Eq. (7)], it is possible to calculate an apparent mobility by combining this approximate ballistic mobility with the intrinsic mobility calculated via Eq. (8) or Eq. (9). In Fig. 12 we present the results of this derived apparent mobility along with the apparent mobility calculated using the average velocity method. We find that the resistance scaling method results and the average velocity method results are consistent with each other throughout the temperature range investigated for both electrons and holes. This confirms that the average velocity method calculates an apparent mobility, which encompasses diffusive and ballistic effects.

The ballistic approximation method can be compared with the resistance scaling analysis as both methods attempt to extract the diffusive scattering component of the mobility. Figure 13 presents the mobilities calculated using both methods for electrons and holes. We find that the

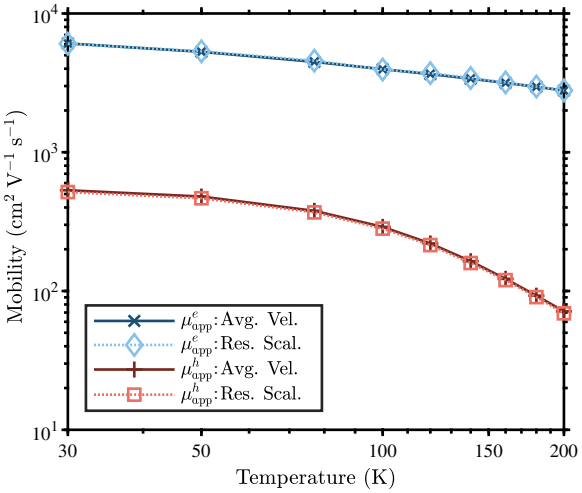

FIG. 12. The electron (dark blue line with x's) and hole (dark blue line with pluses) apparent vertical mobility plotted as a function of temperature calculated using the average velocity method. Also included are the apparent vertical mobilities calculated by combining diffusive and ballistic components using Matthiessen's rule derived from resistance scaling analysis for electrons (light blue dotted line with diamonds) and holes (light red dotted line with squares). These results correspond with simulation sizes of 200 nm. The mobility extracted from the average velocity method is demonstrated to incorporate ballistic and diffusive effects.

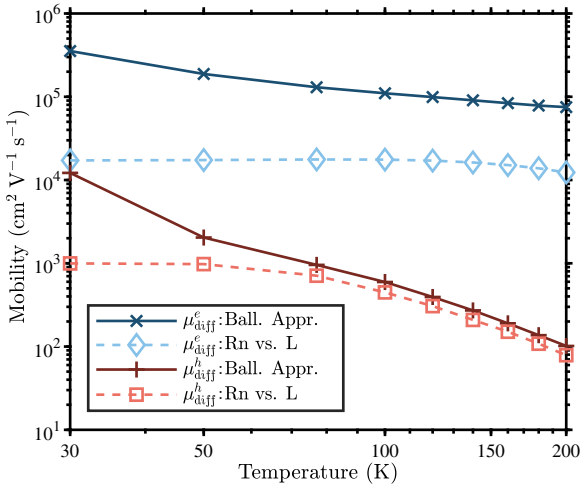

FIG. 13. The diffusive vertical electron and hole mobility as a function of temperature calculated using both resistance scaling analysis [Eq. (9)] and the ballistic approximation method [Eq. (7)] from 200-nm simulations. These results suggests that both methods may be valid for holes at higher temperatures, but not for electrons.

ballistic approximation method compares favorably to the resistance scaling method for holes at temperatures above 100 K, which demonstrates that the inherent approximations of the ballistic approximation method are reasonable. However, at lower temperatures the results for holes are inconsistent. Similar to the results for hole at low temperatures, those for electrons differ dramatically throughout the entire temperature range.

E. Implications for device performance predictions

Given that NEGF calculations are limited computationally to relatively small domains, the results from our study have significant implications for the use of the calculations to predict device properties. For a calculation where the entire structure can be included in the simulation domain, the average velocity method of calculating mobility will result in an apparent mobility that incorporates both ballistic and diffusive components affecting the transport, see Sec. III D, and the overall transport may be well described for this device. However, when a device is too large to simulate with NEGF, the average velocity method may be misleading under certain conditions. To help facilitate this concept, we calculate the ballistic mobility as a function of device length using Eq. (11) for a temperature of 77 K and the conduction band effective mass of InAs (0.023 [59]). Then, assuming an intrinsic mobility of 50 000 cm^2 V^{-1} s^{-1} (estimated for electrons in InAs at 77 K with a density of 1.7×10^{16} cm^{-3} [60]), we calculate the apparent mobility using Eq. (7) and plot the results in Fig. 14. The apparent mobility in a smaller structure is demonstrated to be dominated by the ballistic component. However, a larger structure is dominated by the diffusive-limited component of mobility, because the ballistic component has increased dramatically due to the increase in device size. Thus, the mobility calculated using the average velocity method (apparent mobility) in a smaller simulation may not represent the mobility in a real device. When trying to predict the mobility in a device using this method, the results are only valid when the entire device is modeled in the simulation domain or when the simulation is in the transport regime limited by diffusive processes.

To exemplify how the mobility extraction methodology can affect device performance predictions, we use the Einstein relation along with a minority carrier lifetime τ of 100 ns [61] to estimate the minority carrier diffusion length L_A and the internal quantum efficiency (QE) using Eq. (33) on page 676 of Ref. [62] for an absorption layer thickness W_A of 5 μm. We choose an absorption coefficient α of 500 cm^{-1}, which is artificially low in the case of MWIR InAs/GaSb SLs but may be reasonable for LWIR Ga-free SLs, to better illustrate the impact that the different mobility calculation methods may have on the prediction of device performance. The calculated QE values as a function of temperature are plotted in Figs. 15(a) and 15(b) for hypothetical minority electron and minority hole PDs, respectively. While the approximated QE as a function of temperature for a minority hole PD are fairly consistent between methods, the values for a minority electron PD

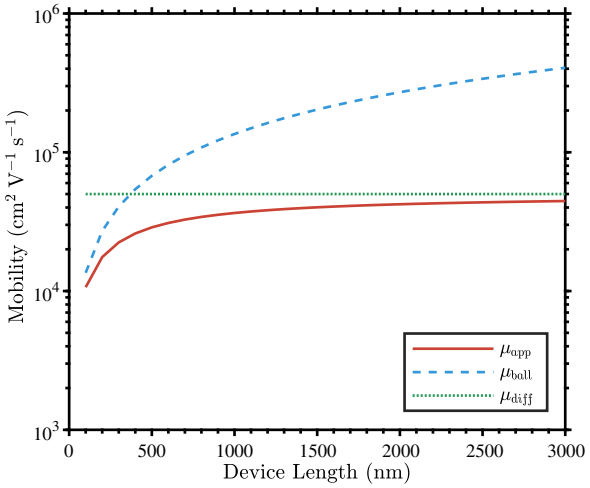

FIG. 14. The apparent, ballistic, and diffusive-limited mobilities calculated for an example InAs device at 77 K as a function of device length. It is clear that the apparent mobility for a smaller device significantly underestimates the mobility in a larger device.

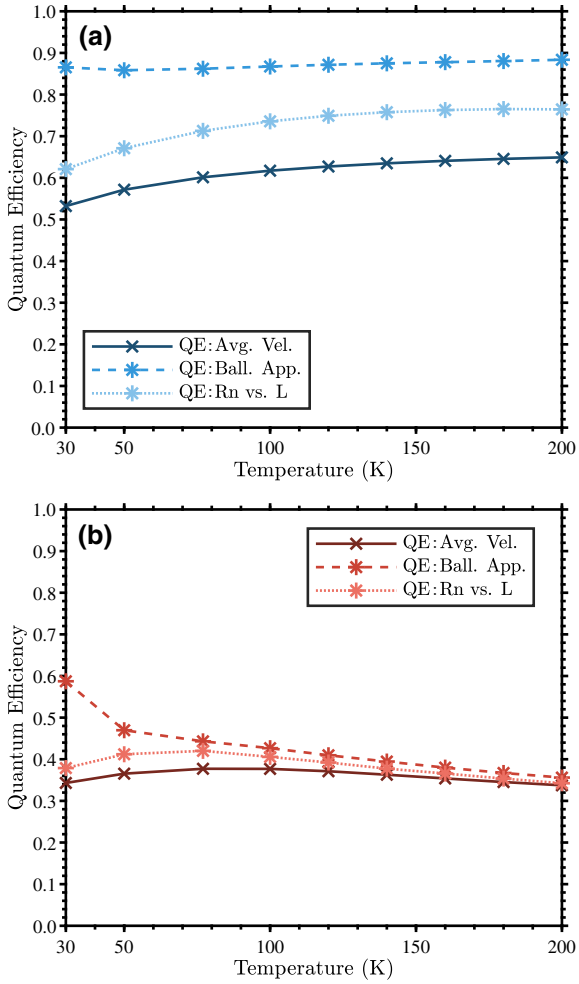

FIG. 15. The approximate quantum efficiency calculated for an electron-based (a) and hole-based (b) T2SL photodetector. The inconsistency between the QEs calculated using the different methods is commensurate with that of the mobilities, exemplifying the impact that mobility extraction methodology can have on predictions of device performance.

vary significantly. This is expected as the results are commensurate with the variation in mobilities calculated using the different methods. As a specific example, choosing the mobility extracted from the average velocity method underestimates the QE for an electron-based PD at 140 K by approximately 16 % of the value calculated using the resistance scaling mobility.

Therefore, predicting device mobility from a nanometer-scale simulation using the average velocity method may not be appropriate in all situations, and is likely only applicable in cases where the resistance scaling method is also valid and transport is dominated by diffusive processes. Regarding the ballistic approximation method, we show that this approximation may be valid in the regime investigated for holes at temperatures above 100 K, but it is inconsistent with the resistance scaling method results for electrons at all investigated temperatures. Ultimately, the resistance scaling method is the only one for which the validity can be inherently determined. Furthermore, the apparent mobility in a T2SL device of arbitrary length can be approximated using the intrinsic mobility and Eq. (13) along with Eq. (7), as in Fig. 14. Resistance scaling provides the most straightforward results demonstrating the utility of the method, but in cases of significant scattering the average velocity might be reasonable and is more computationally efficient. In cases where the simulation is not large enough for resistance scaling to be valid, the ballistic approximation method or the average velocity method can be attempted. However, the limitations of each method must be carefully considered.

IV. CONCLUSION

We investigate the extraction of mobilities from NEGF calculations of T2SLs using the average velocity, the ballistic approximation, and resistance scaling methodologies. It is demonstrated that the average velocity method results in the apparent mobility that encompasses both ballistic and diffusive effects. Thus, the validity of this method as a predictor of device performance is limited to simulations in which the entire device can be simulated or in which transport is dominated by diffusive processes. On the other hand, the ballistic approximation and resistance scaling methods are designed to extract the scattering-limited mobility. The mobilities extracted for holes using both methods are consistent at higher temperatures, but the hole mobilities at low temperatures as well as the electron mobilities for all temperatures are

inconsistent. However, due to the inherent validity of the resistance scaling method, the inconsistency of results demonstrates the tenuous validity of the ballistic approximation method under certain conditions. We employ an alternative method for extracting mobility using resistance scaling when the carrier density is not constant between calculations. This method is demonstrated to produce the same results as the traditional resistance scaling method for holes. For electrons, where the carrier density is less consistent between simulations at different temperatures, this alternative method enabled the extraction of a diffusive mobility from sufficiently long simulations that is independent of simulation size, as would be expected for an intrinsic mobility. Therefore, we are able to extract valid intrinsic mobilities for electrons and holes in the temperature range investigated that can be used to model T2SL behavior in larger devices. These findings are applicable to materials outside of T2SLs and demonstrate that consideration of the physical interpretation of the mobilities extracted using the different methods is important in cases where ballistic transport is significant.

ACKNOWLEDGMENTS

The work at Boston University is supported in part by the Defense Advanced Research Projects Agency (DARPA) Focal Arrays for Curved Infrared Imagers (FOCII) program (Grant No. N66001-20-C-4011), managed by Dr Whitney Mason. Furthermore, the authors would like to thank Dr. Minh Nguyen, Dr Mark O'Masta, and Dr Philip Klipstein for many fruitful discussions.

APPENDIX A: 3D BULK BALLISTIC MOBILITY

We solve for the ballistic mobility of a 3D bulk [Eq. (11)] by following the methods of Lundstrom and colleagues for the calculation of the conductance and ballistic mobility for two-dimensional bulk devices [63,64]. We start with the expression for the conductance in the Landauer formalism [63]:

$$G = \frac{2q^2}{h} \int \mathcal{T}(E) M(E) \left(-\frac{\partial f_0}{\partial E}\right) dE, \tag{A1}$$

where the partial derivative of the Fermi function, f_0, comes from the Taylor expansion of the difference of the Fermi levels between contacts, $\mathcal{T}$ is the transmission function at energy, E, M is the number of conducting channels between contacts, q is the elementary charge, and h is Plank's constant. Next, using the standard expression for the 3D conductance [63] $\sigma_{\text{app}} = GL/A$ in combination with Eq. (A1) we find

$$\sigma_{\text{app}} = \frac{2q^2}{h} \int (\mathcal{T}(E)L) \left(\frac{M(E)}{A}\right) \left(-\frac{\partial f_0}{\partial E}\right) dE. \tag{A2}$$

As pointed out by Lundstrom and Sun, this conductivity should be thought of as an "apparent conductivity" in the case of ballistic transport, as the definition of conductivity is generally applied in the diffusive limit [64]. Similarly, the apparent mobility, μ, can be extracted based on the relationship between mobility and conductivity in the diffusive limit: $\sigma_{\text{app}} = nq\mu_{\text{app}}$, where n is the carrier density in the device. Combining this expression with Eq. (A2) we derive an expression for the apparent mobility for a 3D bulk device:

$$\mu_{\text{app}} = \frac{2q/h}{n} \int (\mathcal{T}(E)L) \left(\frac{M(E)}{A}\right) \left(-\frac{\partial f_0}{\partial E}\right) dE, \tag{A3}$$

Using the expression for the number of conducting modes in a 3D device given in Ref. [63] and the fact that the transmission function is equal to unity for ballistic transport, Eq. (A3) can be rewritten to represent the ballistic mobility as follows:

$$\mu_{\text{ball}} = \frac{2q/h}{n} L \left(\frac{m^*}{2\pi\hbar^2}\right) (K_B T) \frac{\partial}{\partial \eta_F} \int \frac{d\epsilon}{e^{(\epsilon-\eta_F)}+1} d\epsilon, \tag{A4}$$

where m^* is the effective mass, K_B is the Boltzmann constant, T is the temperature, $\hbar$ the reduced Plank's constant, and with substituted variables $\epsilon = (E - E_c)/(K_B T)$ and $\eta_F = (E_F - E_c)/(K_B T)$ where E_c and E_F are the conduction band and Fermi energies, respectively. Using the rules for Fermi integrals as given by Lundstrom and Jeong [63], we can simplify Eq. (A4) to the following:

$$\mu_{\text{ball}} = \frac{2q/h}{n} L \left(\frac{m^*}{2\pi\hbar^2}\right) (K_B T)\, \mathcal{F}_0(\eta), \tag{A5}$$

where F_0 is the Fermi-Dirac integral of order zero. To derive the final expression for the apparent mobility, we first derive an expression for the carrier density. We start with the equation for carrier density in 3D bulk materials [63]:

$$n = \int D_{3\text{D}} f_0(E_F) dE, \tag{A6}$$

where $D_{3\text{D}}$ is the 3D density of states. Inserting the expression for the 3D density of states given in Ref. [63] we find

$$n = \frac{\sqrt{2\,(m^* K_B T)^3}}{\pi^2 \hbar^3} \int \frac{d\epsilon^{1/2}}{e^{(\epsilon-\eta_F)}+1} d\epsilon. \tag{A7}$$

Using the definition for the Fermi integral of one-half order, $F_{1/2}$, we get our final expression for carrier density:

$$n = \frac{\sqrt{2\,(m^* K_B T)^3}}{\pi^2 \hbar^3} \frac{\sqrt{\pi}}{2} \mathcal{F}_{1/2}(\eta_F). \tag{A8}$$

We insert Eq. (A8) into Eq. (A5) to derive our final expression for ballistic mobility:

$$\mu_{\text{ball}} = \frac{L v_T}{2\,(K_B T/q)} \frac{\mathcal{F}_0(\eta_F)}{\mathcal{F}_{1/2}(\eta_F)}, \tag{A9}$$

which corresponds with Eq. (11) of Sec. III A. We insert the unidirectional thermal velocity, $v_T = \sqrt{2k_B T/(\pi m^*)}$, into Eq. (A9).

APPENDIX B: 3D BULK BALLISTIC RESISTANCE

We solve for the ballistic resistance [Eq. (10)] of a 3D bulk material in a similar manner as Eq. (A9) in Abstract A by starting with the reciprocal of the expression for conductivity in the Landauer formalism (A1):

$$R = 1/G = \frac{h}{2q^2}\left(\int \mathcal{T}(E)M(E)\left(-\frac{\partial f_0}{\partial E}\right)dE\right)^{-1}. \tag{B1}$$

Using the definition of the Fermi integral, the expression for the number of conducting channels in a 3D device [63], and the fact that the transmission function is equal to unity for ballistic transport, Eq. (B1) can be transformed as follows:

$$R_{\text{ball}} = 1/G = \frac{h}{2q^2}\frac{2\pi\hbar^2}{m^* K_B T}\left(\frac{\partial}{\partial \eta_F}\int \frac{\epsilon}{e^{\epsilon-\eta_F}}d\epsilon\right)^{-1}. \tag{B2}$$

We use the rules for Fermi integrals provided in Ref. [63] to simplify the expression:

$$R_{\text{ball}} = \frac{h}{2q^2}\frac{2\pi\hbar^2}{m^* K_B T}\frac{1}{\mathcal{F}_0(\eta_F)}. \tag{B3}$$

Finally, we substitute in the expression for the carrier density [Eq. (A8)] to derive the final form of the expression for ballistic resistance as given in Sec. II C:

$$R_{\text{ball}} = \frac{\sqrt{2\pi m^* K_B T}}{nq^2}\frac{\mathcal{F}_{1/2}(\eta_F)}{\mathcal{F}_0(\eta_F)}. \tag{B4}$$

[1] S. Datta, *Quantum Transport: Atom to Transistor* (Cambridge University Press, Cambridge, 2005).

[2] B. Witzigmann, A. Witzig, and W. Fichtner, A multidimensional laser simulator for edge-emitters including quantum carrier capture, IEEE Trans. Electron Devices **47**, 1926 (2000).

[3] C. de Falco, E. Gatti, A. L. Lacaita, and R. Sacco, Quantum-corrected drift-diffusion models for transport in semiconductor devices, J. Comp. Phys. **204**, 533 (2005).

[4] M. G. Ancona and A. Svizhenko, Density-gradient theory of tunneling: Physics and verification in one dimension, J. Appl. Phys. **104**, 073726 (2008).

[5] A. Tibaldi, F. Bertazzi, M. Goano, R. Michalzik, and P. Debernardi, Venus: A vertical-cavity surface-emitting laser electro-opto-thermal numerical simulator, IEEE J. Select. Topics Quantum Electron. **25**, 1 (2019).

[6] A. Tibaldi, J. A. Gonzalez Montoya, M. Vallone, M. Goano, E. Bellotti, and F. Bertazzi, Modeling Infrared Superlattice Photodetectors: From Nonequilibrium Green's Functions to Quantum-Corrected Drift Diffusion, Phys. Rev. Appl. **16**, 044024 (2021).

[7] D. N. Arnold, G. David, D. Jerison, S. Mayboroda, and M. Filoche, Effective Confining Potential of Quantum States in Disordered Media, Phys. Rev. Lett. **116**, 056602 (2016).

[8] M. Filoche, M. Piccardo, Y.-R. Wu, C.-K. Li, C. Weisbuch, and S. Mayboroda, Localization landscape theory of disorder in semiconductors. I. Theory and modeling, Phys. Rev. B **95**, 144204 (2017).

[9] S. Poli and M. G. Pala, Channel-length dependence of low-field mobility in silicon-nanowire FETs, IEEE Electron Device Lett. **30**, 1212 (2009).

[10] S. Poli, M. G. Pala, and T. Poiroux, Full quantum treatment of remote Coulomb scattering in silicon nanowire FETs, IEEE Trans. Electron Devices **56**, 1191 (2009).

[11] M. G. Pala, C. Buran, S. Poli, and M. Mouis, Full quantum treatment of surface roughness effects in silicon nanowire and double gate FETs, J. Comp. Electron. **8**, 374 (2009).

[12] M. Luisier, Phonon-limited and effective low-field mobility in n- and p-type [100]-, [110]-, and [111]-oriented Si nanowire transistors, Appl. Phys. Lett. **98**, 032111 (2011).

[13] M. Aldegunde, A. Martinez, and A. Asenov, Non-equilibrium Green's function analysis of cross section and channel length dependence of phonon scattering and its impact on the performance of Si nanowire field effect transistors, J. Appl. Phys. **110**, 094518 (2011).

[14] M. Frey, A. Esposito, and A. Schenk, Computational comparison of conductivity and mobility models for silicon nanowire devices, J. Appl. Phys. **109**, 083707 (2011).

[15] V.-H. Nguyen, F. Triozon, F. D. R. Bonnet, and Y.-M. Niquet, Performances of strained nanowire devices: Ballistic versus scattering-limited currents, IEEE Trans. Electron Devices **60**, 1506 (2013).

[16] R. Rhyner and M. Luisier, Phonon-limited low-field mobility in silicon: Quantum transport vs. linearized boltzmann transport equation, J. Appl. Phys. **114**, 223708 (2013).

[17] Y.-M. Niquet, V.-H. Nguyen, F. Triozon, I. Duchemin, O. Nier, and D. Rideau, Quantum calculations of the carrier mobility: Methodology, Matthiessen's rule, and comparison with semi-classical approaches, J. Appl. Phys. **115**, 054512 (2014).

[18] V.-H. Nguyen, Y.-M. Niquet, F. Triozon, I. Duchemin, O. Nier, and D. Rideau, Quantum modeling of the carrier mobility in FDSOI devices, IEEE Trans. Electron Devices **61**, 3096 (2014).

[19] F. Bertazzi, A. Tibaldi, M. Goano, J. A. G. Montoya, and E. Bellotti, Nonequilibrium Green's Function Modeling of Type-II Superlattice Detectors and its Connection to Semiclassical Approaches, Phys. Rev. Appl. **14**, 014083 (2020).

[20] E. Bellotti, F. Bertazzi, A. Tibaldi, J. Schuster, J. Bajaj, and M. Reed, Disorder-Induced Degradation of Vertical Carrier Transport in Strain-Balanced Antimony-Based Superlattices, Phys. Rev. Appl. **16**, 054028 (2021).

[21] M. Shur, Low ballistic mobility in submicron HEMTs, IEEE Electron Device Lett. **23**, 511 (2002).

[22] J. Wang and M. Lundstrom, Ballistic transport in high electron mobility transistors, IEEE Trans. Electron Devices **50**, 1604 (2003).

[23] K. Huet, J. Saint-Martin, A. Bournel, S. Galdin-Retailleau, P. Dollfus, G. Ghibaudo, and M. Mouis, in *ESSDERC 2007 - 37th European Solid State Device Research Conference* (IEEE, Munich, 2007), p. 382.

[24] M. Zilli, D. Esseni, P. Palestri, and L. Selmi, On the apparent mobility in nanometric n-MOSFETs, IEEE Electron Device Lett. **28**, 1036 (2007).

[25] E. Gnani, A. Gnudi, S. Reggiani, and G. Baccarani, Effective mobility in nanowire FETs under quasi-ballistic conditions, IEEE Trans. Electron Devices **57**, 336 (2010).

[26] M. A. Riyadi and V. K. Arora, The channel mobility degradation in a nanoscale metal–oxide–semiconductor field effect transistor due to injection from the ballistic contacts, J. Appl. Phys. **109**, 056103 (2011).

[27] V. K. Arora, in *Proceedings of the 19th International Conference Mixed Design of Integrated Circuits and Systems - MIXDES 2012* (IEEE, Warsaw, 2012), p. 17.

[28] S. Guarnay, F. Triozon, S. Martinie, Y.-M. Niquet, and A. Bournel, in *2014 International Conference on Simulation of Semiconductor Processes and Devices (SISPAD)* (IEEE, Yokohama, Japan, 2014), p. 105.

[29] J. Lusakowski, W. Knap, Y. Meziani, J. Cesso, A. El Fatimy, R. Tauk, N. Dyakonova, G. Ghibaudo, F. Boeuf, and T. Skotnicki, in *Proceedings of 35th European Solid-State Device Research Conference, 2005. ESSDERC 2005.* (IEEE, Grenoble, France, 2005), p. 561.

[30] J. Łusakowski, M. J. M. Martínez, R. Rengel, T. González, R. Tauk, Y. M. Meziani, W. Knap, F. Boeuf, and T. Skotnicki, Quasiballistic transport in nanometer Si metal-oxide-semiconductor field-effect transistors: Experimental and Monte Carlo analysis, J. Appl. Phys. **101**, 114511 (2007).

[31] R. Wang, H. Liu, R. Huang, J. Zhuge, L. Zhang, D.-W. Kim, X. Zhang, D. Park, and Y. Wang, Experimental investigations on carrier transport in Si nanowire transistors: Ballistic efficiency and apparent mobility, IEEE Trans. Electron Devices **55**, 2960 (2008).

[32] L. Liu, V. Saripalli, V. Narayanan, and S. Datta, in *2011 International Electron Devices Meeting* (IEEE, Washington, DC, 2011), p. 4.5.1.

[33] J. J. Gu, H. Wu, Y. Liu, A. T. Neal, R. G. Gordon, and P. D. Ye, Size-dependent-transport study of $In_{0.53}Ga_{0.47}As$ gate-all-around nanowire MOSFETs: Impact of quantum confinement and volume inversion, IEEE Electron Device Lett. **33**, 967 (2012).

[34] A. Majumdar and D. A. Antoniadis, Analysis of carrier transport in short-channel MOSFETs, IEEE Trans. Electron Devices **61**, 351 (2014).

[35] J. Lin, Y. Wu, J. A. del Alamo, and D. A. Antoniadis, Analysis of resistance and mobility in InGaAs quantum-well MOSFETs from ballistic to diffusive regimes, IEEE Trans. Electron Devices **63**, 1464 (2016).

[36] K. Huet, D. Querlioz, W. Chaisantikulwat, J. Saint-Martin, A. Bournel, M. Mouis, and P. Dollfus, Monte Carlo study of apparent magnetoresistance mobility in nanometer scale metal oxide semiconductor field effect transistors, J. Appl. Phys. **104**, 044504 (2008).

[37] A. Rogalski, P. Martyniuk, and M. Kopytko, InAs/GaSb type-II superlattice infrared detectors: Future prospect, Appl. Phys. Rev. **4**, 031304 (2017).

[38] D. Z.-Y. Ting, A. Soibel, L. Höglund, J. Nguyen, C. J. Hill, A. Khoshakhlagh, and S. D. Gunapala, in *Advances in Infrared Photodetectors*, Semiconductors and Semimetals, Vol. 84, edited by S. D. Gunapala, D. R. Rhiger, and C. Jagadish (Elsevier, 2011), p. 1.

[39] J. Bajaj, G. Sullivan, D. Lee, E. Aifer, and M. Razeghi, in *Infrared Technology and Applications XXXIII*, Vol. 6542, edited by B. F. Andresen, G. F. Fulop, and P. R. Norton, International Society for Optics and Photonics (SPIE, Orlando, Florida, 2007), p. 65420B.

[40] A. Rogalski, P. Martyniuk, and M. Kopytko, Type-II superlattice photodetectors versus HgCdTe photodiodes, Progress Quantum Electron. **68**, 100228 (2019).

[41] B. V. Olson, J. F. Klem, E. A. Kadlec, J. K. Kim, M. D. Goldflam, S. D. Hawkins, A. Tauke-Pedretti, W. T. Coon, T. R. Fortune, E. A. Shaner, and M. E. Flatté, Vertical Hole Transport and Carrier Localization in $InAs/inas_{1-x}sb_x$ Type-II Superlattice Heterojunction Bipolar Transistors, Phys. Rev. Appl. **7**, 024016 (2017).

[42] L. K. Casias, C. P. Morath, E. H. Steenbergen, G. A. Umana-Membreno, P. T. Webster, J. V. Logan, J. K. Kim, G. Balakrishnan, L. Faraone, and S. Krishna, Vertical carrier transport in strain-balanced InAs/InAsSb Type-II superlattice material, Appl. Phys. Lett. **116**, 182109 (2020).

[43] L.-W. Wang, S.-H. Wei, T. Mattila, A. Zunger, I. Vurgaftman, and J. R. Meyer, Multiband coupling and electronic structure of $(InAs)_n/(GaSb)_n$ superlattices, Phys. Rev. B **60**, 5590 (1999).

[44] P. Enders, A. Bärwolff, M. Woerner, and D. Suisky, $k \cdot p$ theory of energy bands, wave functions, and optical selection rules in strained tetrahedral semiconductors, Phys. Rev. B **51**, 16695 (1995).

[45] U. Aeberhard, Ph.D. thesis, Eidgenössische Technische Hochschule Zürich, 2008.

[46] M. Luisier, A. Schenk, W. Fichtner, and G. Klimeck, Atomistic simulation of nanowires in the $sp^3d^5s^*$ tight-binding formalism: From boundary conditions to strain calculations, Phys. Rev. B **74**, 205323 (2006).

[47] S. Steiger, Ph.D. thesis, Eidgenössische Technische Hochschule Zürich, 2009.

[48] D. Esseni and F. Driussi, A quantitative error analysis of the mobility extraction according to the Matthiessen rule in advanced MOS transistors, IEEE Trans. Electron Devices **58**, 2415 (2011).

[49] *MATLAB version 9.9.0.1592791 (R2020b) Update 5*, The Mathworks, Inc., Natick, Massachusetts (2020).

[50] A. Aalok, Professional plots, https://www.mathworks.com/matlabcentral/fileexchange/100766-professional˙plots (2021), [Online; accessed October 31, 202].

[51] I. Vurgaftman, J. R. Meyer, and L. R. Ram-Mohan, Band parameters for III–V compound semiconductors and their alloys, J. Appl. Phys. **89**, 5815 (2001).

[52] See Supplemental Material at http://link.aps.org/supplemental/10.1103/PhysRevApplied.19.044045 for a description of the simulation parameters used and additional information that, while not necessary for understanding the

findings of the paper, may provide additional value for the interested reader.

[53] We choose a higher electric field in the case of electrons as we find that electron transport is highly coherent, but we confirm that the apparent mobility is reasonably consistent in this range (see Supplementary Material [52]). Inelastic scattering will result in the smoothing of spectral functions, so in the absence of adequate scattering the required number of energy integration points can be prohibitively large [17].

[54] B. V. Olson, L. M. Murray, J. P. Prineas, M. E. Flatté, J. T. Olesberg, and T. F. Boggess, All-optical measurement of vertical charge carrier transport in mid-wave infrared InAs/GaSb type-II superlattices, Appl. Phys. Lett. **102**, 202101 (2013).

[55] S. S. Li, Investigation of electronic transport, recombination and optical properties in $InAs_{1-x}P_x$ alloy systems, Final Report, Dec. 1973 - Apr. 1976 Florida Univ., Gainesville. Engineering and Industrial Experiment Station. (1976).

[56] C. H. Swartz and T. H. Myers, Method for the simultaneous determination of vertical and horizontal mobilities in superlattices, Phys. Rev. B **89**, 075305 (2014).

[57] We use the data from the 100-, 150-, and 200-nm simulations for mobilities at 77 K and the 200- and 250-nm simulations for below 77 K.

[58] Specifically, we use the data from the calculations with lengths of 200, 250, 300, 350, and 400 nm.

[59] W. Nakwaski, Effective masses of electrons and heavy holes in GaAs, InAs, A1As and their ternary compounds, Physica B **210**, 1 (1995).

[60] D. Rode, *Chapter 1 Low-Field Electron Transport* (Elsevier, Amsterdam, 1975), p. 1.

[61] D. Donetsky, G. Belenky, S. Svensson, and S. Suchalkin, Minority carrier lifetime in type-2 InAs–GaSb strained-layer superlattices and bulk HgCdTe materials, Appl. Phys. Lett. **97**, 052108 (2010).

[62] S. M. Sze, *Physics of Semiconductor Devices* (Wiley-Interscience, Hoboken, NJ, 2007), 3rd ed.

[63] M. Lundstrom and C. Jeong, *Near-Equilibrium Transport* (World Scientific Publishing Company, Singapore, 2013).

[64] M. Lundstrom and X. Sun, Some useful relations for analyzing nanoscale mosfets operating in the linear region (2016), https://arxiv.org/abs/1603.03132.